Identifying optimal microwave frequencies to detect floating macroplastic litter using machine learning

Tomás Soares da Costa[1], João Felício[1], Mário Vala[2], Rafael Caldeirinha[2], Sergio Matos[1,3], Jorge Costa[1,3], Carlos Fernandes[1] (ORCID), Nelson Fonseca[4] and Peter de Maagt[5]

[1]Instituto de Telecomunicações, Instituto Superior Técnico, Universidade de Lisboa, Lisbon, Portugal; [2]Instituto de Telecomunicações, School of Technology and Management, Polytechnic University of Leiria, Leiria, Portugal; [3]Departamento de Ciências e Tecnologias da Informação, Instituto Universitário de Lisboa (ISCTE-IUL), Lisbon, Portugal; [4]Anywaves, Toulouse, France and [5]Antenna and Sub-Millimetre Waves Section, European Space Agency (ESA), Noordwijk, The Netherlands

Abstract

Microwaves (MWs) have emerged as a promising sensing technology to complement optical methods for monitoring floating plastic litter. This study uses machine learning (ML) to identify optimal MW frequencies for detecting floating macroplastics (>5 cm) across S, C, and X-bands. Data were obtained from dedicated wideband backscattering radio measurements conducted in a controlled indoor scenario that mimics deep-sea conditions. The paper presents new strategies to directly analyze the frequency domain signals using ML algorithms, instead of generating an image from those signals and analyzing the image. We propose two ML workflows, one unsupervised, to characterize the difference in feature importance across the measured MW spectrum, and the other supervised, based on multilayer perceptron, to study the detection accuracy in unseen data. For the tested conditions, the backscatter response of the plastic litter is optimal at X-band frequencies, achieving accuracies up to 90% and 80% for lower and higher water wave heights, respectively. Multiclass classification is also investigated to distinguish between different types of plastic targets. ML results are interpreted in terms of the physical phenomena obtained through numerical analysis, and quantified through an energy-based metric.

CAMBRIDGE UNIVERSITY PRESS

Introduction

Several million tons of mismanaged plastic waste are dumped in the oceans yearly, and its volume has been growing exponentially over the past few years. Plastic litter is present in all shapes and sizes from meters, down to the nanoscale. Its lingering presence, either floating or submerged, is dangerously affecting the marine ecosystem, ultimately having direct impact on the human food chain. The pressing concern of marine plastic pollution has captured the interest of numerous researchers [1, 2].

Over the past decade, several studies focusing on detection strategies for marine macroplastics have been reported [3–6]. The bulk of these initial studies focuses on the use of optical and hyperspectral data. More recently, detection strategies employing machine learning (ML) algorithms have surfaced. This is explained by the increasing availability of open-source datasets [7–9]. ML models may improve, or supplement existing strategies in ocean monitoring tasks given their higher flexibility and capability of recognizing meaningful patterns in complex environments. This is of particular importance in monitoring deep-sea environment, where the sea state rapidly changes. However, current research has shown that environmental impairments common in deep-sea such as shadowing, sun glint and overall weather conditions can deteriorate detection performance when using optical and hyperspectral instruments.

Motivated by the development of an all-weather monitoring system, recent studies have investigated the detection of marine plastic litter, i.e., floating macroplastics (>5 cm), using microwaves (MWs) [10–15]. MWs do not suffer from major atmospheric impairments and have been used as a remote sensing technology for several science and Earth observation missions. A radar-based metric was suggested recently for remote detection of floating plastic litter, the energy ratio (*EnR*) [11]. This metric is based on the backscattered energy response of the floating macroplastic targets, mainly produced by the concave and meniscus indentations that the objects create on the water surface. However, the *EnR* formulation requires two conditions to get

detection in a certain scenario: (1) reference measurements of the water without the presence of the floating macroplastics, to establish a detection threshold; and (2) sequential measurements capturing the drift of the targets in the observed scene. Both conditions severely hamper the possibility of performing close to real-time detection.

There is a notable gap in the literature as none of these initial studies has investigated the use of ML algorithms on MW backscattered signal data to gain additional insight on the surface response with and without floating macroplastics, or whether it is possible to perform detection directly on the measured frequency domain signals without producing an image. In contrast to the physical approach, the newly supervised ML workflow proposed in this paper requires no reference measurement right before target presence, neither sequential target measurement. With ML automation, we obtain an adaptive detection method that is more suitable for close to real-time monitoring. Additionally, it requires less bandwidth than the *EnR* approach for similar performance and can work with noncontiguous frequency bands.

Available research has already shown the advantages of using ML algorithms to analyze MW remote sensing experimental data in multiple other ocean monitoring and detection applications [16]. Xiang et al. [17] demonstrated the use of ML models, e.g., random forest and an artificial neural network (ANN), to improve sea surface wind speed estimation using data from a MW scatterometer and radiometer together. Gao et al. [18] used another ML model, support vector machines (SVMs), to estimate significant wave height from Synthetic Aperture Radar (SAR) imagery data. A similar study was presented by Krinitskiy et al. [19] using ship-based radar imagery data and ANNs to estimate the significant wave height. ANNs and SVMs are also widely used to perform detection of sea ice [20] and ships [21] using satellite-borne pol-SAR imagery data from different MW bands.

Data is key in ML and, thus, the choice of a suitable operating band for the MW sensing instrument plays a vital role in obtaining quality results. Contrary to the previous applications, the task of monitoring floating macroplastic is still at its infancy; hence, the choice of an appropriate MW frequency to separate the plastic response from the water surface still requires investigation. Small single-use plastic items typically produce a weak MW response [14]. In contrast, the sea surface has a high scattering response, given its high electric permittivity ($\varepsilon_r \approx 64 @ 4\,GHz$) and conductivity ($\sigma \approx 9.8 @ 4\,GHz$) [22]. This means that scattering from the plastic litter is often engulfed in the overwhelming scattering from the water surface. To exacerbate the problem, floating macroplastics are typically found scattered around the ocean in low concentrations [23]. This makes it even more challenging to separate the water surface and plastic responses, to detect its presence. Hence, determining the optimal MW frequency to isolate the plastic response becomes even more crucial.

To the authors' best knowledge, this work is the first to use ML algorithms to explore experimental MW backscattered data of water surfaces with and without floating macroplastics to, ultimately, determine the optimal MW frequency across S-, C-, and X-bands for its detection. Using ML to evaluate MW data at signal level allows for a fast analysis, directly from the MW instrument, that can complement existing detection strategies using optical or hyperspectral data.

We conducted wideband S-, C-, and X-bands backscattering radio measurements (from 2.5 to 11.5 GHz) in a controlled indoor environment at DELTARES facilities (NL) [24], that mimics deep-sea wave conditions. The measured datasets describe a statistically identical, time-evolving water surface with and without a low concentration ($10\,g/m^2$) of spread out floating macroplastics.

An earlier version of this paper was presented at the 18th Conference of Antennas and Propagation (EuCAP 2024) and was published in its Proceedings [25]. In that preliminary version, we carried out an unsupervised ML workflow to characterize the experimental frequency dependency scattering behavior in the presence of the spread out plastic targets. Our proposed methodology computed the difference between the total importance of a selected sub-band within an MW interval from datasets with and without plastic targets, *Reference* and *Target*, respectively. Here, we complement our previous exploratory data analysis by (1) performing numerical analysis and simulation work to deepen the study of the MW effects, i.e., analyze the frequency selective scattering behavior of floating macroplastics; (2) studying identical test cases in higher water wave heights conditions; (3) adding a supervised ML workflow to compute the detection accuracy and identify the optimal MW frequencies; (4) comparing the supervised ML model performance considering narrower bandwidths with an alternative detection metric (*EnR*); and (5) evaluating the possibility of using ML to distinguish, statistically, between different plastic targets, i.e., performing multiclass classification.

This paper is organized as follows: The "ML methodology" section presents the ML models used in the two proposed workflows; the "Data workflow" section describes the data workflow, which includes the data acquisition, preprocessing, analysis, and detection metrics; the "Results and discussion" section presents the numerical analysis and simulation work, the experimental results obtained in the two dynamic water conditions using the two ML workflows, and the comparison of using supervised ML with an alternative detection metric; lastly, main conclusions are drawn in the "Conclusions" section.

ML methodology

Predominantly, two main types of ML approaches are typically used to study a problem: a descriptive or unsupervised learning approach occurs when we are given unlabeled data, $\boldsymbol{x}$, and the goal is to unveil hidden patterns within the dataset. Each data input x_i consists of a vector of p independent variables called features; a predictive or supervised learning approach, where the goal is to learn a mapping from inputs $\boldsymbol{x}$ to the corresponding outputs $\boldsymbol{y}$ given a set of input–outputs pairs commonly known as training data (or inputs). Once trained, we can then use the model to make predictions ($\hat{\boldsymbol{y}}$) for unseen inputs.

In the context of floating macroplastics detection, the predictive approach is framed as a binary classification problem. Here, the model assigns labels "0" and "1" to unseen inputs, representing the absence or presence of floating macroplastics, negative and positive responses, respectively. The model estimates the conditional probability $p(\boldsymbol{y}|\boldsymbol{x})$, which quantifies the likelihood of a given input x_i belonging to either class. In this section, we describe the ML algorithms used in both unsupervised and supervised learning workflows.

Principal component analysis

Principal component analysis (PCA) is one of the most widely used techniques in tabular, multivariate dataset analysis and is employed primarily for dimensionality reduction [26, 27]. Implementation wise, PCA can be easily implemented through singular value

decomposition (SVD) [28]. Therefore, no implementation difficulties were encountered when processing the Electromagnetic (EM) data which is, inherently, complex-valued. Hence, when applying PCA to an MW tabular dataset, we directly used the complex-valued measurements of the scattering parameters.

In essence, PCA extracts a lower dimensional feature set that explains most of the variability of the original dataset. The k extracted features, or principal components, PC_is, are (each) a linear combination of the original features (X_j) scaled by a loading value ($\alpha_{ij} \in \mathbb{C}$). This process of combining original features is often also referred to as feature extraction. The loading values represent the importance that each original feature has in the formation of a PC. For example, α_{ij} indicates the degree of importance, or contribution, of the original jth feature in the ith PC. Mathematically, each ith PC is written as follows [29]:

$$PC_i = \alpha_{i1}X_1 + \alpha_{i2}X_2 + ... + \alpha_{ip}X_p \,, \tag{1}$$

Each PC explains a proportion of the total variance of the dataset at hand. Since the PCs are calculated to preserve the maximum energy content of the data matrix, i.e., variance, the first PC always explains the most variance, the second PC always explains the second most variance, and so on. However, in the presence of a large number of original features, the consideration of only the first few PCs may be insufficient to account for most of the variability in the data. Thus, in this work, dimensionality is reduced to account for 95% of the total explained variance.

In the context of MW application, SVD is widely used as a powerful filter to block reflections from stronger scatterers [30]. With PCA, we obtain a multidimensional coordinate system that reveals the underlying linear energy trends of the data set. Following Parseval's Relation, this means that we maintain capability of filtering the reflections of the higher energy scatterers from the interpretable time domain intensity function (see the "Physical-based detection metric" subsection further ahead) while having the interpretation possibility in the frequency domain through the loadings of each PC, i.e., a clear understanding of the contribution of an original variable to a certain PC.

From the relation of the extracted features with the original ones described above in Eq. (1), the absolute value of the loadings can statistically evaluate the contribution of the ith frequency component to the feature extraction result. The magnitude of this contribution represents the feature importance estimation associated to the dataset at hand [27]. Since each PC explains a proportion of the total variance, it is appropriate to weight each contribution by the respective proportion of explained variance, π_i [26]. This can be referred to as weighted PCA (WPCA) FS algorithm in which we can compute the importance (c) of the jth feature as follows:

$$c_j = \sum_{i=1}^{k} |\alpha_{ij}| \pi_i, k = 1, 2, ..., p \quad , \tag{2}$$

where k is the total number of PCs retained and π_i is the corresponding weight of the ith PC. Concatenating together the importances of all the features, we obtain the frequency importance vector of a certain MW *dataset*, $c_{dataset}$.

From Eq. (2), we can interpret that, in MW applications, by summing the contributions from consecutive frequencies within an arbitrary sub-band interval, we can determine its total importance, $C_{sub-band}$. Mathematically, for the measured N_f frequencies within the chosen sub-band, its total importance is computed as in Eq. (3). To improve filtering and focus on the central frequency, we also apply a Hamming window (H) to the importance interval.

$$C_{sub-band} = \sum_{f=1}^{N_F} H\left(c_f\right) \tag{3}$$

Multilayer perceptron artificial neural networks

For classification model, we use a multilayer perceptron (MLP) [31]. The advantages are threefold: First, it has been shown in [32] that, if well-tuned, its performance on tabular datasets is on par, accuracy-wise, with other ML algorithms commonly used to process tabular datasets (e.g., SVM, XGBoosts, and Gradient-Based Decision Trees). We verify that the use of the MLP model in the supervised learning workflow (see the "Supervised learning workflow" subsection further ahead) is superior to other tuned ML algorithms; Second, it serves as a baseline to develop more intricate neural network (NN) architectures for specific applications; Third, it is possible to implement this architecture in the complex domain (contrary to other ML algorithms) and directly process the complex-valued MW measurement data [33].

In Fig. 1, we can observe an overview of the MLP architecture, with a neuron unit highlighted in blue (for visualization purposes), used to make a prediction on the magnitude of a 1D scattering parameter signal, S_{11}. At least three layers make up an MLP architecture: an input layer, an output layer, and one or more intermediate layers, commonly referred to as hidden layers (HLs), which define the depth of the NN [31]. The signal information flows from the input layer to the output layer.

The input layer neuron units directly take the values of the input features. Both the depth and number of neurons in each HL can be optimized as explained further ahead in the "Supervised learning workflow" subsection. For classification tasks, the output layer consists of n_c neurons where n_c is the number of classes. In binary classification specifically, we can use a single output neuron.

A neuron consists of a weighted sum of inputs from the previous layer and a bias parameter, to which is then applied a (nonlinear) activation function. Each neuron in the fully connected layers is connected to all neurons in the preceding layer. In a vectorized notation, an arbitrary output from the neurons of a fully connected layer, $\boldsymbol{h^i}$, in an MLP is computed as

$$\boldsymbol{h^i} = \sigma\left(W^i h^{i-1} + b^i\right), \tag{26}$$

where W^i is the weight matrix, b^i is the bias vector, σ is the activation function and h^{i-1} is the output from a previous layer.

It is the sequential application of the nonlinear activation function in the layer's neurons, σ, that enable even shallow MLPs to learn complicate patterns of the data. The optimal activation function for the neurons in the HLs depends on the training (application) data and is typically determined empirically. For practically all test cases, the model selected from the fine-tuning process (see Appendix) uses ReLU [33] as the activation function of the neurons in the HLs. Only in the output layer do we specifically required an activation function that outputs the probability distribution over the different classes. For this we used the softmax function [31].

The pattern recognition ability of MLPs is realized via supervised training. In this process, all the weights and bias parameters (denoted as W^i and b^i, respectively) are continuously updated to ensure that the network output matches with the desired output based on the given labels of the training data. However, for each training input, there is still an error between the predicted output and the target one. This error evaluates the performance of our classifier and is quantified by a loss function, E. Since this is
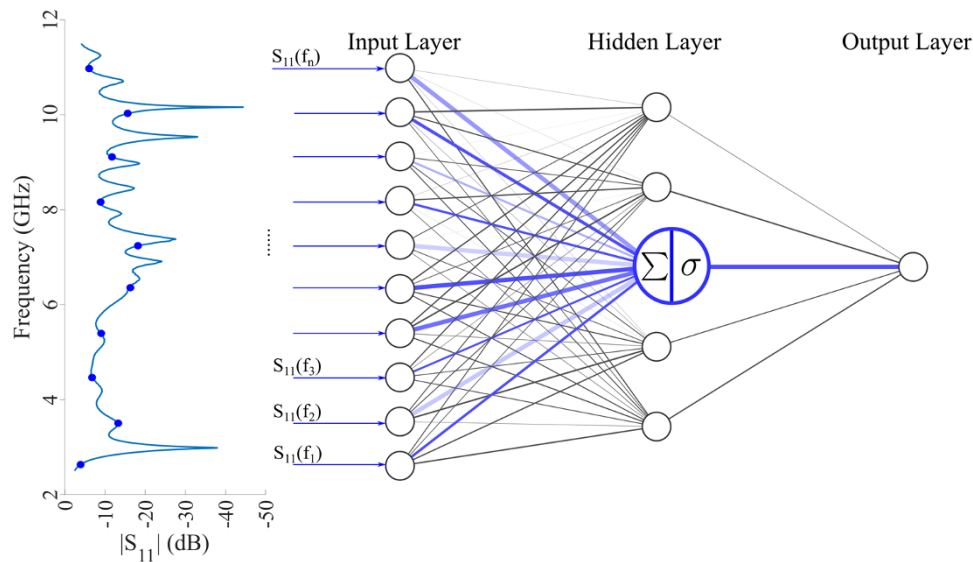
Figure 1. Overview of the MLP architecture used to process a 1D signal consisting of the magnitude of a scattering parameter, S_{11} (for visualization purposes). A neuron unit is highlight in blue.

a classification task, we used the cross-entropy loss [31] as our loss function. The network parameters are trained by using stochastic gradient descent (SGD) and backpropagation. SGD is an optimization method that minimizes the cost of the error loss function by updating the network parameters with the error gradient from a small, randomly selected set of training inputs. Backpropagation is used to compute the error gradients of each pair of network parameters in the MLP, $\partial E/\partial W$ and $\partial E/\partial b$, respectively. Accordingly, the update rule for both weights and biases follows $W \leftarrow W - (\partial E/\partial W)$, where η is the learning rate. The reader is referred to the works in papers [31] and [33] for further details on the training algorithms.

The extension of the MLP model to the complex domain does not alter its architecture and employs the same formulation as described earlier. The main changes are in its capacity (e.g., the number of neurons) and the implementation of nonlinear functions to handle complex-valued data types [34]. However, the network's output still needs to be mapped to a real-valued label, i.e., real domain. The mapping of complex to real ($\mathbb{R} \rightarrow \mathbb{C}$), through magnitude, can be done either at the input or the output layer [33]. This flexibility to compare the two types of architecture allows us to determine, empirically, the optimal placement of the mapping layer and selection of the optimal data type for our scattering parameter data during the fine-tuning process.

Data workflow

In this section, we describe the signal data workflow, beginning with its acquisition in the dynamic water scenarios of the measurement campaign, followed by its preprocessing and analysis using the two proposed ML workflows. Finally, we introduce the alternative physical-based detection metric used for comparison with the proposed supervised ML approach.

Acquisition

The most common types of plastic that end up as marine litter are single-use items, containers and wrappers, like bottles, styrofoams, etc. [23]. As previously referred, these low mass, single-use plastic
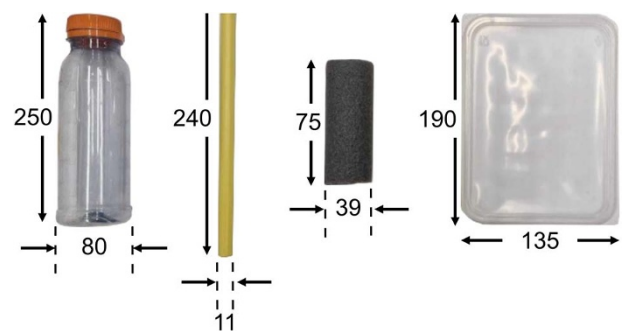

Figure 2. Low permittivity plastic litter targets measured. From left to right: plastic bottle ($\varepsilon_r \approx 3.4$), plastic straw ($\varepsilon_r \approx 2.1$), cylinder foam ($\varepsilon_r \approx 1.6$), and plastic lid ($\varepsilon_r \approx 2.2$). Dimensions in millimeters.

items are typically found scattered in deep-sea. These items are made of low permittivity polymers such as polypropylene (PP), polyethylene terephthalate (PET), and polystyrene (PS) [35]. In Fig. 2, we show the single-use plastic items used in the measurement campaign. From left to right: PET plastic bottle ($\varepsilon_r \approx 3.4$); PP plastic straw ($\varepsilon_r \approx 2.1$); PS cylinder foam ($\varepsilon_r \approx 1.6$); and PP plastic lid ($\varepsilon_r \approx 2.2$).

A measurement campaign was conducted at the 75×8.5 m water basin, inside a closed pavilion, at DELTARES facilities [24]. This facility replicates water surfaces in near-deep-sea conditions. The waves are generated by computer-controlled wave paddles that produce a moving water surface according to a JONSWAP spectrum defined *a priori* [36]. This wave spectrum can be generated according to two parameters that characterize the water surface system: significant wave height H_s; and peak wave period T_p. For the purpose of this study, we considered an identical wave spectrum with $H_s = \{9;17\}$ cm and $T_p = 1.2$ s across all test cases. An illustrative example corresponding to the 9 cm case is presented in Fig. 3(a).

The measurement setup is represented in Fig. 3(b). It consisted of a monostatic setup with a single V-pol reflector antenna mounted 9 m above the water level on an existing wooden walkway, to approach a typical satellite look angle. Vertical polarization to
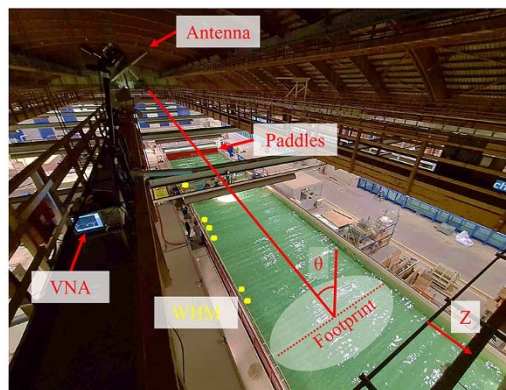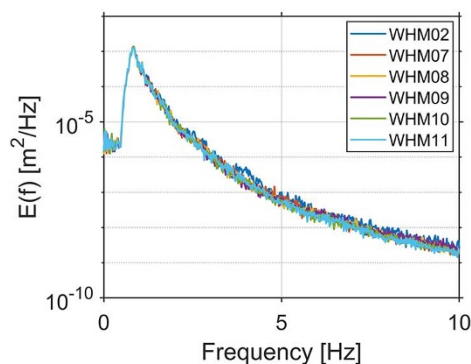
Figure 3. Indoor controllable scenario: (a) JONSWAP wave spectrum measured at several wave gauges (WHM) that ensured a water surface with $H_s = 9$ cm and $T_p = 1.2$ s throughout the basin; (b) measurement setup surveying middle of the basin.

transmit and receive the MW signal (VV) was selected to maximize the plastic target's response at MW frequencies. The antenna was pointing at a common point on the water surface, approximately 7.64 m away from the antenna, with a 38° incidence angle (θ). It was operating in pure backscatter mode whilst connected to the first port of an Agilent E5071C Vector Network Analyzer that measures the frequency response (S_{11}) between 2.5 and 11.5 GHz with 1601 equally spaced points. Each frequency sweep had a time duration of approximately 1 s. The water waves travel along the antenna's cross-range direction, the Z-axis in the aforementioned figure.

Measurements always started without any objects in the water (reference measurements) and continued while and after plastic litter was added. The plastic targets drifted within the footprint (target measurements) following the water wave's direction of propagation, Z. For each test case, we attempted to keep a constant concentration of 10 g/m^2. However, since the items are dropped at the beginning of the basin, near the wave paddles, they sometimes accumulated and created intermittent litter patches across the antenna's footprint. This varies the backscatter intensity level in the sequential target measurements.

The experimental data is arranged as a tabular dataset where each input is one of the sequential measurements, i.e., a discretized backscattering S_{11} frequency sweep, and its features correspond to the MW response sampled at the subsequent frequency points (f_i) within the measured spectrum. Considering that we have video footage of every test case, we filter and divide each MW measurement dataset into two identical tabular datasets composed of n units and p features for reference and target measurements, *Reference* and *Target*, respectively. In every test case, both the *Reference* and *Target* datasets had, roughly, around 400 measurements with 1601 frequency points between 2.5 and 11.5 GHz. Lastly, we label each *Reference* signal as class "0" and each *Target* signal as class "1."

Analysis and detection

Next, we describe the signal preprocessing routine, and the subsequent unsupervised and supervised learning workflows to characterize the experimental frequency dependency scattering behavior in the presence of the spread out plastic targets and identify the optimal MW frequencies for detection, respectively.

Signal preprocessing

To obtain an accurate measured backscatter response, we apply a background subtraction calibration method. This operation also removes all responses from undesired stationary scatterers (e.g., basin walls). Since the water surface is a stochastic process, this is computed by subtracting the mean response of the reference measurements [10]. In a real deployment, there would be practically no stationary targets in the open sea, so the signal could be directly processed from the MW sensing instrument.

To ensure that we consider the frequency response of just the water surface within the antenna's footprint, we apply distance gating to every S-parameter signal to remove any clutter leftover from the mean reference subtraction. Figure 4 summarizes the steps of this preprocess and subsequent calculation of the time domain *EnR* metric (see the "Physical-based detection metric" subsection further ahead). For every reference and target measurement, we compute its inverse Fast Fourier Transform (IFFT) to obtain the time-domain (radar) response, I_{ij}; gate the radial distances outside the basin limits of the field of view; and then re-apply an FFT to obtain the corresponding, footprint frequency MW response. We use the interval between [10;15] m as radial distances.
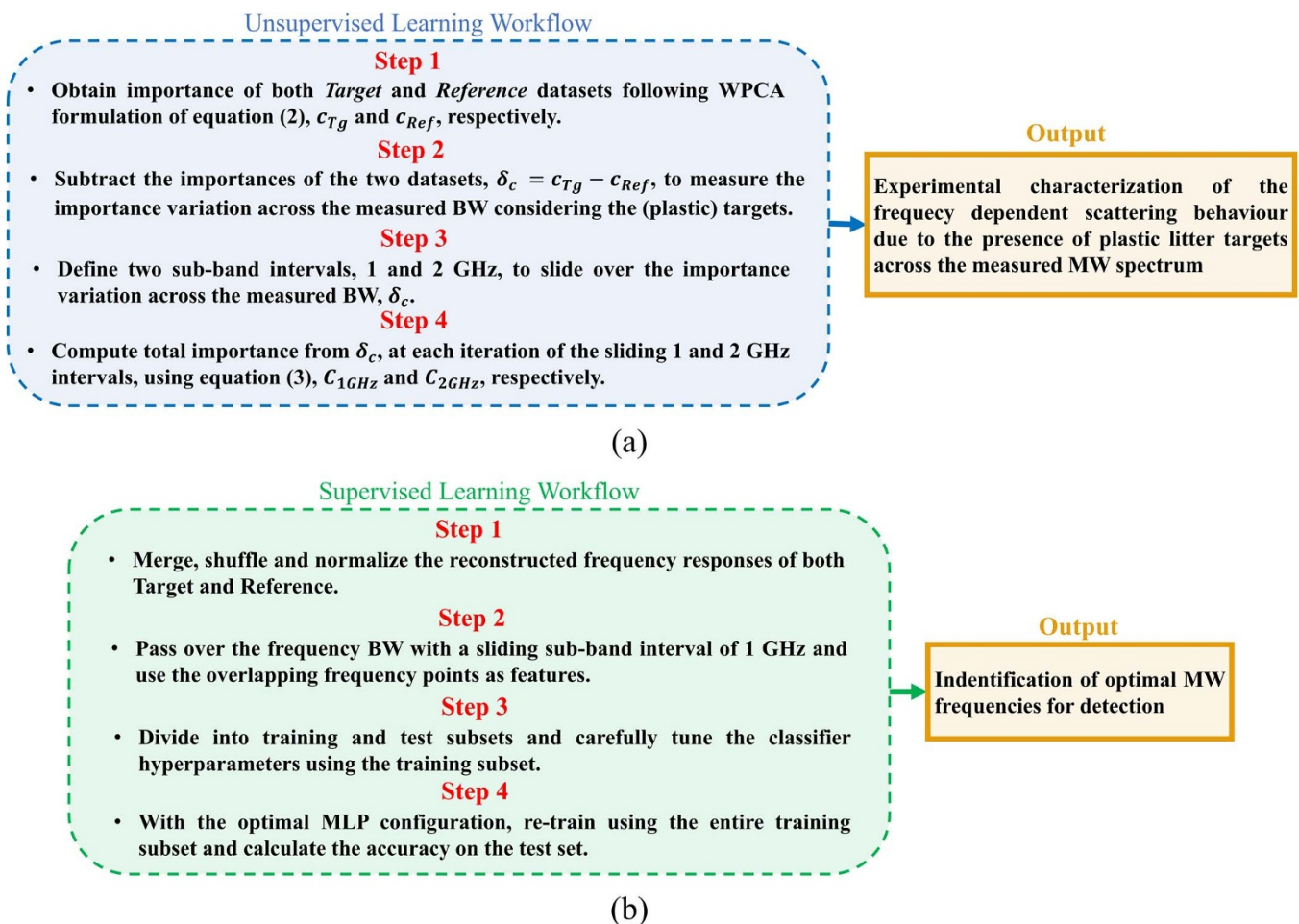
Unsupervised learning workflow

Following the previous data preprocessing routine, we first describe the unsupervised learning workflow from our preliminary work [25], summarized in Fig. 5(a). The goal of this workflow is to characterize, experimentally, the difference in importance of each MW frequency across the measured spectrum when considering the presence of the floating macroplastic targets. First, we compute and concatenate the feature importance at each frequency point for the *Target* and *Reference* datasets using the WPCA algorithm described in Eq. (2) to obtain c_{Target} and $c_{Reference}$ (or, for short, c_{Tg} and c_{Ref}), respectively (step 1). We then subtract c_{Ref} to c_{Tg} to obtain the difference in feature importance between the two datasets, $\delta_c = c_{Tg} - c_{Ref}$, to gauge the difference in importance variation across the measured BW when considering the presence of the floating plastic targets (step 2). Next, we define two sub-bands intervals, with 1 and 2 GHz of bandwidth, to slide over the importance variation from the previous step, δ_c (step 3). At each iteration of the sliding 1 and 2 GHz window, we compute the total importance from δ_c using Eq. (3), using the N_f frequency points within the window, to obtain C_{1GHz} and C_{2GHz} (step 4).

Supervised learning workflow

We complement the previous unsupervised learning workflow with a supervised learning workflow, shown in Fig. 5(b), to identify the optimal MW frequencies for detection of the floating macroplastic targets. First, we merge, shuffle and normalize
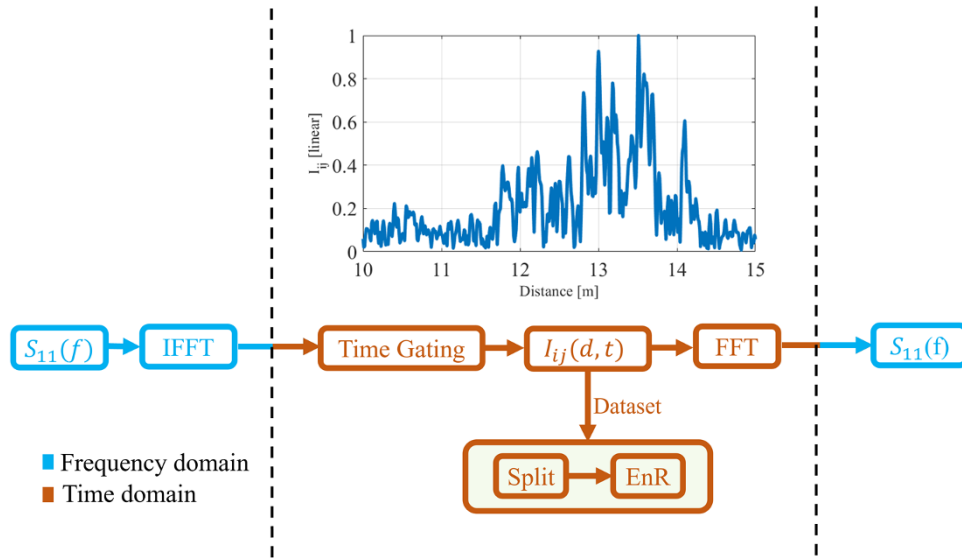
Figure 4. Preprocessing signal routine to remove clutter leftover from the mean reference subtraction and subsequent derivation of *EnR* metric (see the "Physical-based detection metric" subsection).

Unsupervised Learning Workflow

Step 1
- Obtain importance of both *Target* and *Reference* datasets following WPCA formulation of equation (2), c_{Tg} and c_{Ref}, respectively.

Step 2
- Subtract the importances of the two datasets, $\delta_c = c_{Tg} - c_{Ref}$, to measure the importance variation across the measured BW considering the (plastic) targets.

Step 3
- Define two sub-band intervals, 1 and 2 GHz, to slide over the importance variation across the measured BW, δ_c.

Step 4
- Compute total importance from δ_c, at each iteration of the sliding 1 and 2 GHz intervals, using equation (3), C_{1GHz} and C_{2GHz}, respectively.

Output

Experimental characterization of the frequecy dependent scattering behaviour due to the presence of plastic litter targets across the measured MW spectrum

(a)

Supervised Learning Workflow

Step 1
- Merge, shuffle and normalize the reconstructed frequency responses of both Target and Reference.

Step 2
- Pass over the frequency BW with a sliding sub-band interval of 1 GHz and use the overlapping frequency points as features.

Step 3
- Divide into training and test subsets and carefully tune the classifier hyperparameters using the training subset.

Step 4
- With the optimal MLP configuration, re-train using the entire training subset and calculate the accuracy on the test set.

Output

Indentification of optimal MW frequencies for detection

(b)

Figure 5. Machine learning workflows: (a) unsupervised; (b) supervised.

the magnitude of the reconstructed frequency responses of both *Target* and *Reference* datasets (step 1). We use the previous sliding sub-band with an interval of 1 GHz to sweep the 10-GHz BW. In each iteration, we use the N_f frequency points within the window as features for our classifier (step 2). We divide the full dataset into training and test subsets (80/20 ratio, respectively) and carefully

Table 1. *EnR* detection thresholds of 9 and 17 cm waves for S-, C-, and x-bands

Frequency band	f_1 (GHz)	f_2 (GHz)	EnR_9^{th}	EnR_{17}^{th}
S	2.5	4	1.24	1.27
C	4	8	1.29	1.37
X	8	11.5	1.46	1.52

Table 2. Regulated EESS frequency intervals used in this study [38]

Frequency interval	f_1 (GHz)	f_2 (GHz)
$EESS_3$	3.1	3.3
$EESS_5$	5.25	5.57
$EESS_9$	9.5	9.8
$EESS_{10}$	9.9	10.4
EESSC	Concatenation of EESS intervals	

fine tune the MLP model's hyperparameters using *Ray Tune* library [37] with the training subset (step 3). The reader is referred to the Appendix for details on the hyperparameter optimization implementation. During the fine-tuning process, the training subset is repeatedly split into several smaller training subsets and corresponding validation subsets due to the use of a cross-validation technique. Finally, we select the optimal MLP model configuration from the fine-tuning step and train the model using the entire training subset – thus leveraging all available labeled data under the chosen hyperparameters – and only then evaluate its performance by computing the accuracy on the test set (step 4).

Accuracy is defined as the number of correct predictions divided by the total number of predictions. A correct prediction implies that the predicted response for an input matches the label. The predictions on unseen data are typically presented in a confusion matrix format, which summarizes the performance of the classification algorithm. It can also provide more details about the misclassifications and the classes that are the most difficult (or easiest) to classify.

To evaluate multiclass classification scenarios, in the first step of the supervised learning workflow, we merge *Target* datasets from the other test cases. To ensure that the multiclass dataset remains balanced, we use an identical number of reference measurements from the corresponding *Reference* datasets. The labels of the *Target* measurements are also adjusted accordingly to the number of classes, and the multiclass accuracy is computed as the mean of the per-class accuracy.

Physical-based detection metric

Lastly, we intend to compare the proposed (supervised) ML approach with an alternative detection metric for floating macroplastics, the *EnR* [10], that closely relates to the physical scattering process. Similarly to accuracy, this metric summarizes the detection performance in a single number but based on the time-varying comparison of the scattering intensity response (i.e., time-domain response, I_{ij}) of the water surface with floating macroplastics and without.

Since we already performed distance gating in the signal preprocessing, we can easily obtain the *EnR* associated with the corresponding dataset from the one-sided IFFT of the input signals (see Fig. 4). *EnR* provides interpretability of the backscatter response, i.e., logic behind the MW measurements, that complements well the ML analysis. Thus, the comparison is justified. Following [10], we define in Table 1 the *EnR* detection thresholds for the 9 and 17 cm wave datasets (EnR_9^{th} and EnR_{17}^{th}, respectively) considering S-, C-, and X-bands. These thresholds are based on the uncertainty of the reference measurement datasets over time.

The two main drawbacks with *EnR* are identified as bandwidth and threshold definition. *EnR* requires large bandwidths, at least in the order of 2 GHz within the C- and X-bands, as it loses interpretability when using smaller bandwidths, e.g., 1 GHz

or below. However, narrower bandwidths are required to comply with the available bands for Earth Exploration Satellite Services (EESS) in active remote sensing. In Table 2, we show existing EESS frequency intervals in S-, C-, and X-bands for active remote sensing applications [38]. *EnR* also requires sequential reference measurements of a certain water state to establish the threshold detection level. This can restrict its application to continuous real-time monitoring, especially considering higher velocity platforms.

Results and discussion

The interaction between plastic litter and water is a challenging problem, particularly when considering small, single-use items with dimensions close to the operation wavelength and negligible plastic mass. In this section, we start with the physical characterization of the problem. We demonstrate, using full-wave simulations, that the small concave and meniscus indentations that the plastic items form on the water surface play an important role in the backscatter frequency response. Then, we escalate the simulation work to one of the dynamic scenarios measured experimentally and analyze the dependency of the backscatter response with varying MW frequency and water wave heights.

Following the simulation work, we analyze the experimental MW data at the signal level using the two proposed ML workflows for every test case in the two water states considered. First, we employ the unsupervised ML workflow to characterize the difference in the frequency dependent scattering behavior across the measured MW spectrum between the two classes of data. Then, we use the supervised ML workflow to identify the optimal MW frequencies for detection within the measured MW spectrum. We also compare the ML-based detection results with the alternative radar-based detection metric and investigate detection using the narrower EESS frequency intervals. Finally, we evaluate the feasibility of performing multiclass classification using ML.

Simulation analysis

To demonstrate the frequency selective behavior of the backscatter produced by the floating plastic items, we consider a 1 × 1 m patch of static water. Floating on the flat surface, we consider the plastic bottle target (see Fig. 2) with thin walls. This object creates a cylindrical indentation on the water surface, with a depth d that is a function of its weight. We carry out full-wave finite difference time-domain (FDTD) simulations for different indentation depths in CST Microwave Studio [39]. In the simulations, we consider an incident plane wave with linear vertical polarization and an incident angle of 37° measured with respect to the horizontal plan.
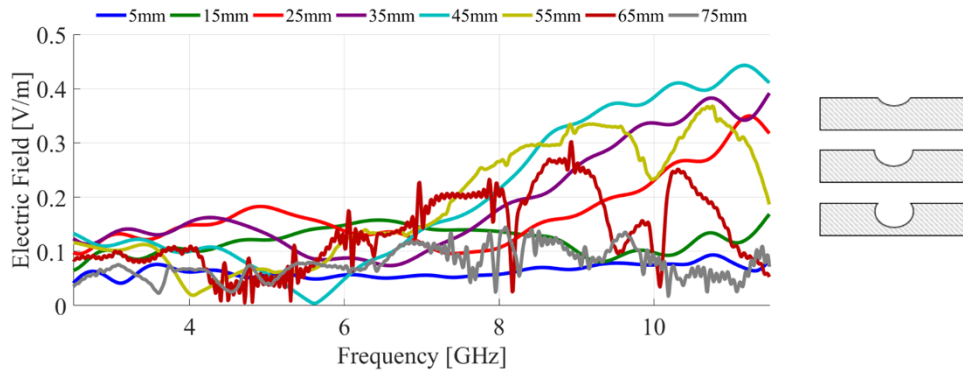
Figure 6. Backscattered electric field of plastic bottle vs frequency with different sinking depths d = {5, 15, 25, 35, 45, 55, 65, 75} mm.

Figure 6 shows the backscattered electric field across the measured MW spectrum for different d values. The results demonstrate a frequency selectivity effect, in which the optimal frequency for the maximum intensity of the backscattered signal varies according to the indentation depth. We also evaluated the field distribution near the indentations. For deeper indentations, the backscatter signal is caused by the resonances due to by "trapped" fields at the edges of the indentation [40]. The results demonstrate a preference for higher MW frequencies, i.e., X-band. This is a consequence of the electrical lengths of the indentations. These interpretations can only be obtained by simulation; however, the total response follows the one obtained experimentally for the same target [10]. Hence, we can conclude that the backscattering signal coming from the low permittivity target depends on the interplay between the indentation depth and the surrounding water surface.

In dynamic water scenarios, the backscatter field produced by the scattered plastic items is mixed with scattering from the surrounding rough surface. Furthermore, the MW backscattering is dependent on several parameters, for instance quantity, individual object geometry, weight, orientation w.r.t incident wave, water surface level, etc. [10]. Some of these can change significantly between consecutive measurements. Hence, in a dynamic scenario, we require multiple measurements to study the frequency selective behavior of the backscattering. The size in terms of wavelength, of a statically presentative sample of this surface demands an unaffordable amount of computational resources for FDTD simulations; therefore, CST's asymptotic numerical solver is used instead.

We simulate the time evolving water surface generated from a JONSWAP spectrum with an H_s of 9 and 17 cm, representing the experimental scenario. The targets are 250-mm plastic bottles represented by their water indentation. The backscatter is calculated across S-, C-, and X-bands multiple times, considering sequentially different locations and orientations of the drifting indentation targets. We calculate Reference and Target datasets in each band (see the frequency interval limits in Table 1). Each simulated backscatter signal is preprocessed with the subtraction of the mean of references (see the "Signal preprocessing" subsection).

As an initial exploratory analysis, we apply PCA, see Eq. (1), to the simulated datasets across S-, C-, and X-bands to observe the data separability. In Fig. 7(a) and 7(b), we represent the clusters of the simulated Reference and Target datasets, for the first two PCs. For each sub-band, we indicate in the figure insets the Euclidean distance between the centroids of the two classes of data.

The distance between the centroids of the Reference and Target classes is larger in the lower water wave height case. The smaller distances between clusters in higher water wave height suggests a deterioration of the detection performance when Hs increases. In fact, we observe in the simulations that the increase in water wave height leads to a higher number of ray bounces (multipath). Hence, in every Target surface, there is an additional backscattering contribution from the higher order reflections that is mixed with the bottles' response. Notably, for this shallow indentation, the backscattered field is described by a specular reflection. Across both water wave height cases, we observe that the increase in MW frequency also increases the distance between clusters, an indication of improved detection performance.

In the next subsection, we will use our unsupervised ML workflow to characterize the experimental frequency dependent scattering behavior across the measured MW spectrum in the presence of the floating macroplastics.
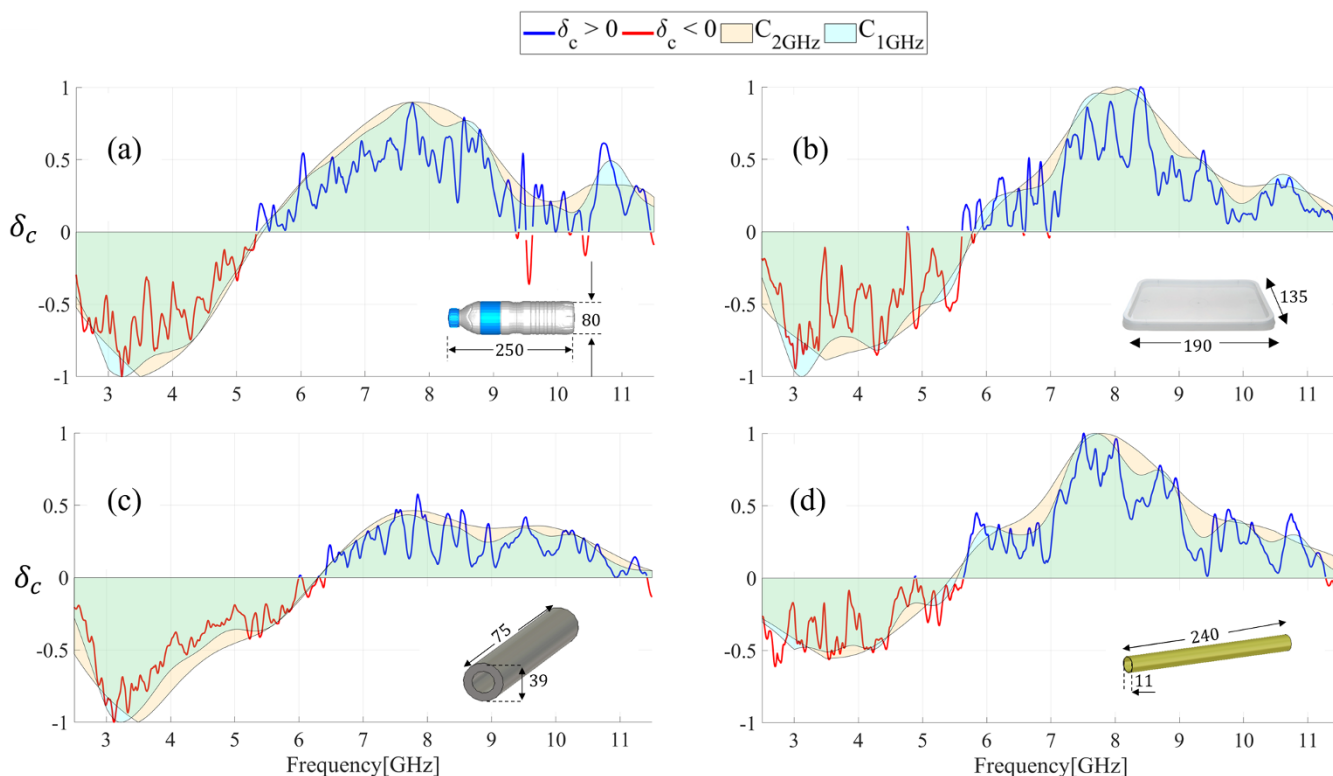
Frequency importance analysis

In our preliminary analysis (see Fig. 3 from paper [25]), we had already analyzed the individual frequency importances of both Target and Reference datasets (c_{Tg} and c_{Ref}, respectively) for all measured cases in 9 cm waves, i.e., output of step 1 of the unsupervised workflow, see Fig. 5(a). For the same test cases in 17 cm waves, the behavior of the c_{Ref} and c_{Tg} curves were identical.

Figures 8 and 9 show the normalized difference in feature importance curves between Target and Reference datasets, δ_c, and the corresponding areas of total importance for the sliding windows of 1 and 2 GHz, C_{1GHz} and C_{2GHz}, for the test cases with an H_s of 9 and 17 cm waves, respectively. This corresponds to the outputs of steps 2 and 4 of the unsupervised workflow. The δ_c curves summarize the prior analysis for the setup at hand, showing that the presence of the floating macroplastic litter leads to an increase of the importance (with $\delta_c > 0$) of upper C- and X-band frequencies (> 6 GHz). For the higher X-band frequencies (around 10 GHz), even though there is a decrease in difference importance, it is still relevant due to the very low importance of c_{Ref} curves. From Eqs (1) and (2), we observe that importance coefficients are scaled by the corresponding PC variance. This means that the principal contributors to the variance of the first PCs, i.e., main scatterers of the surface in each scenario, sway the importance curve. Consequently, the optimal frequencies to denote the presence of the floating plastic targets are on the positive part of the difference curve ($\delta_c > 0$).
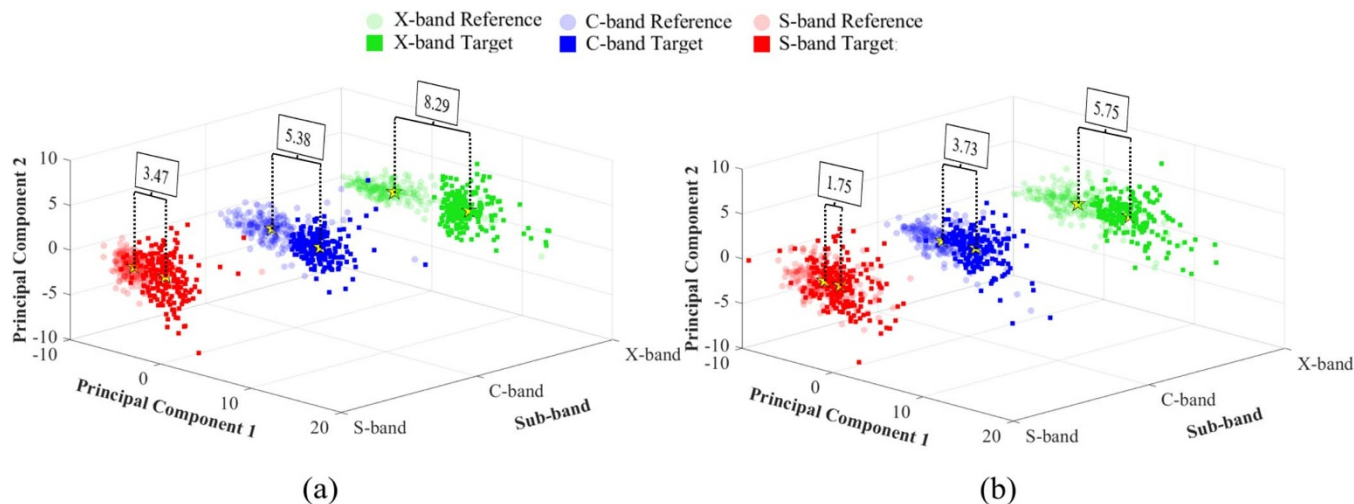
Figure 7. Clusters of simulated *Reference* and *Target* datasets for the plastic bottles test case across S-, C-, and X-bands for an emulated time evolving water surface generated from a JONSWAP spectrum with an H_s of (a) 9 cm; (b) 17 cm. For each sub-band, we show in the insets the Euclidean distance between the centroids of the two classes of data.
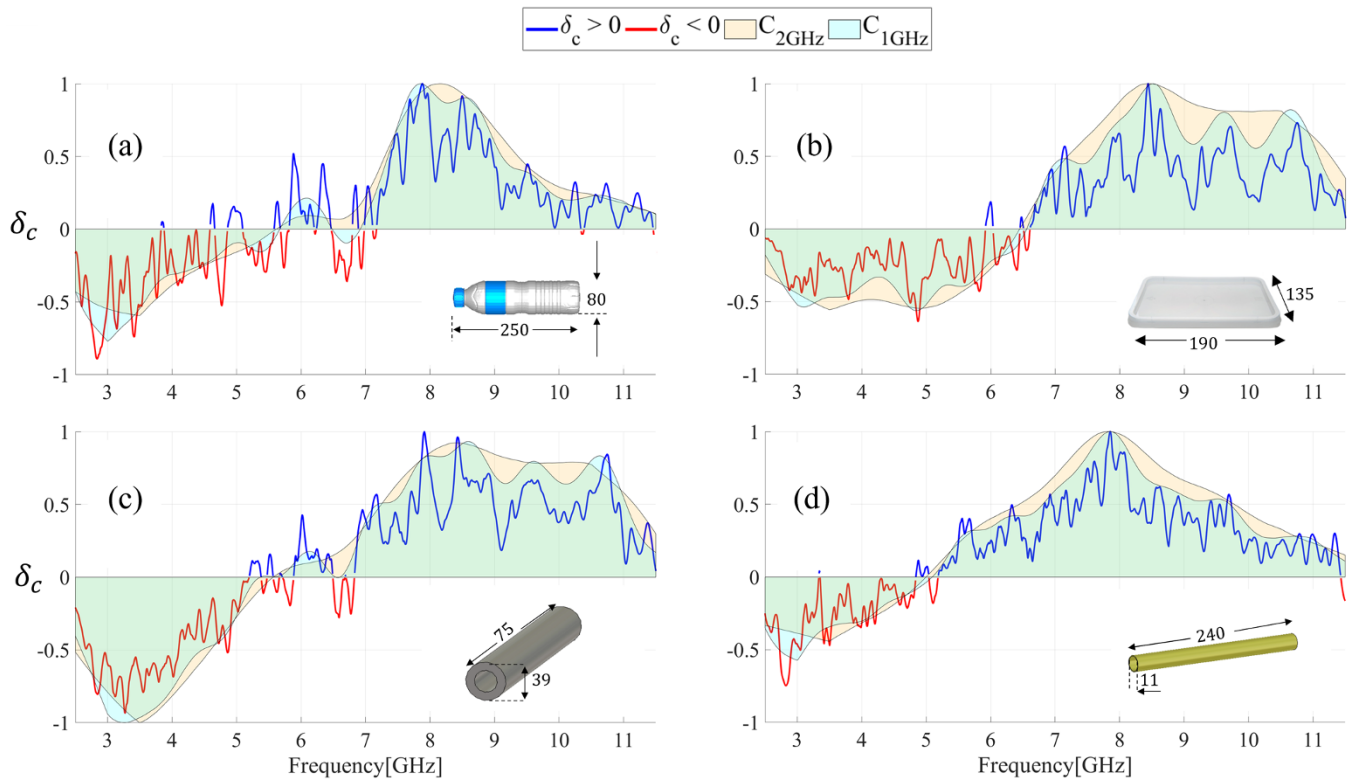

Figure 8. The line shows the normalized difference in frequency importance between the *Target* and *Reference* datasets, δ_c, and the areas represent to the total importances of the sliding 1 and 2 GHz sub-band intervals, C_{1GHz} and C_{2GHz}, for the test cases measured with a water surface height of $H_s = 9$ cm. (a) Plastic bottles; (b) plastic straws; (c) cylinder foams; (d) plastic lids. The inset shows the plastic target's dimensions in millimeters.

Regarding the areas of total importance for the 1 and 2 GHz bandwidth, we observe that using the wider 2 GHz sub-band computes, for the most part, higher total importance. Even with the use of the Hamming window to compute the total importance, this is expected as the C_{2GHz} interval considers more frequencies in the sum. Since 2 GHz is an unrealistic bandwidth to use in real-world applications due to regulatory constraints, we focus on the positive area parts where the $C_{1GHz} \geqslant C_{2GHz}$. For the 9 and 17 cm wave cases, this mainly happens around 8, 9 and 10.5 GHz. Considering the previous simulation results, this further accentuates that X-band frequencies are more relevant for the detection of floating macroplastics.

In the next subsection, we will employ the supervised learning workflow to confirm if this relationship across the wide-band spectrum also points to higher MW frequencies for best detection.

Figure 9. The line shows the normalized difference in frequency importance between the *Target* and *Reference* datasets, δ_c, and the areas represent the total importances of the sliding 1 and 2 GHz sub-band intervals, C_{1GHz} and C_{2GHz}, for the test cases measured with a water surface height of $H_s = 17$ cm. (a) Plastic bottles; (b) plastic straws; (c) cylinder foams; (d) plastic lids. The inset shows the plastic target's dimensions in millimeters.

Detection analysis

We apply the supervised ML workflow to the four test cases measured in the two water wave states. In Fig. 10, we can observe the accuracy output of the binary classification considering 9 (left) and 17 (right) cm wave heights, respectively. Starting with the 9 cm cases, all four test cases lead to a confident detection (above 90%) with upper C- and X-band frequencies. For the plastic bottles, straws, lids, and cylinder foams, the maximum accuracy obtained is 99.05%, 99.45%, 96.51%, and 95.68% at 8, 9, 9.8, and 10.4 GHz, respectively. For the 17 cm wave cases, the maximum accuracy obtained for the same cases is 83.82%, 93.81%, 85.43%, and 88.29% at 8.9, 10.2, 9.3, and 10.4 GHz, respectively. These results show that the frequencies with positive difference in feature importance are in C- and X-bands, which is consistent with the previous unsupervised analysis. Our tuned MLP model learnt the backscatter intensity pattern denoting the presence of floating macroplastic. It successfully discriminated reference measurements from target measurements (and vice-versa), independently of the type of plastic target, through upper C- and X-band frequencies. Thus, we can in fact confirm that the classification of each signal is mainly associated with the strength of targets' backscatter response. Noteworthy, for the worse 17 cm water waves scenario, only with X-band frequencies around 9 and 10 GHz does the accuracy remain above 80% for all test cases. The previous numerical analysis also justifies this result considering that the frequency selective scattering behavior from each individual plastic item contributes with higher backscatter responses at X-band frequencies.

Finally, even though the plastic straws case shows the highest accuracy output along the X-band (especially in the 17 cm water waves), this only means that the target measurements from this class have a more consistent backscatter intensity level at these frequencies. This can be attributed to the much higher number of plastic straws on top of the water surface in contrast to the other heavier plastic items to makeup the continuous concentration of $10\,g/m^2$. This leads to fewer misclassifications when separating from the lower intensity reference measurements.

Comparison with physical-based detection metric

Next, we compare the detection performance of the supervised ML model using the standard EESS frequency intervals (see Table 2) and of the alternative physical-based *EnR* metric, which requires larger bandwidths. First, we investigate detection using the *EnR* metric, quantifying the difference in backscatter intensity produced by the scatterers in the antenna footprint for the *Reference* and *Target* datasets (see the "Physical-based detection metric" subsection for details). Besides the physical interpretability, we can also estimate the impact of higher waves and different MW frequencies in the detection sensitivity. The first three columns in Table 3 presents the *EnR* values for all four test cases with 9 and 17 cm wave height, considering the S-, C-, and X-bands of Table 1. Recall that the *EnR* detection threshold for $H_s = 9\,cm$ is slightly below 1.4 and for $H_s = 17\,cm$ it is slightly below 1.5 (Table 1). While the *EnR* is only slightly above the threshold at S-band, it is much above it for C- and X-band at $H_s = 9\,cm$ and for the X-band at $H_s = 17\,cm$.

Notably, the water surface wave height impacts the detection sensitivity at all MW frequencies. In fact, Table 3 shows that the *EnR* metric decreases across the measured MW spectrum when the water wave height increases. Conversely, when the water wave
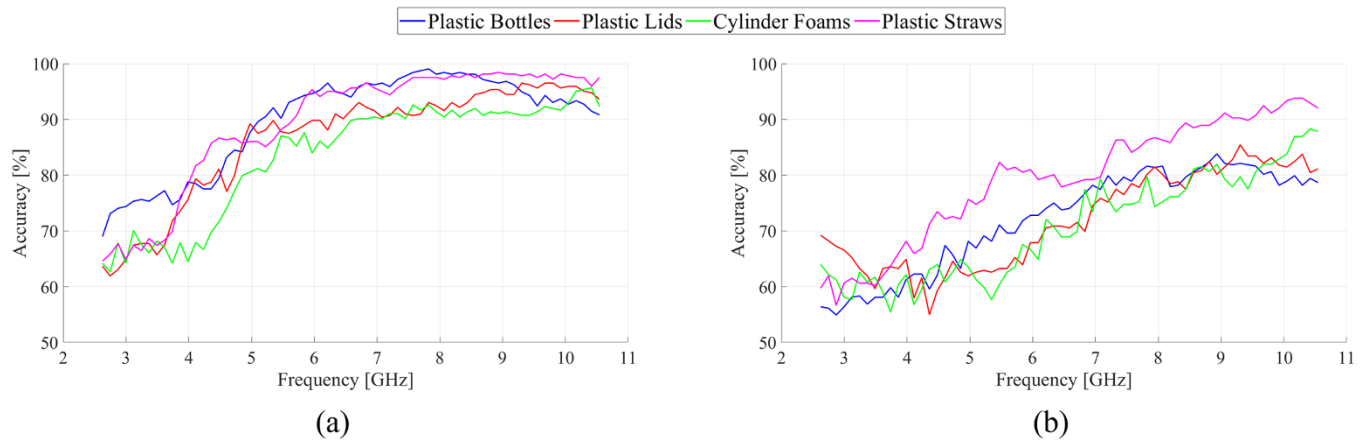
Figure 10. Accuracy output for supervised learning workflow using 1 GHz sub-bands for the test cases with an H_s of (a) 9 cm and (b) 17 cm.

Table 3. Detection values of 9 and 17 cm waves for all four target types across S-, C-, and X-bands using *EnR* and supervised ML to EESS intervals

H_s (cm)	Target	S-band	C-band	X-band	$EESS_3$	$EESS_5$	$EESS_9$	$EESS_{10}$	$EESSc$
9	Bottles	1.6	2.87	2.98	65.1	83.2	92	90.7	91.7
	Straws	1.32	2.37	2.36	62.5	76	92.2	92.1	93.2
	Lids	1.49	2.5	2.81	63.1	77.3	90.4	94.1	92.1
	Cylinder foams	1.75	3.67	4.06	64.7	84.2	94.2	93.9	94.5
17	Bottles	1.14	1.48	2.03	54.9	68.9	79.4	79.1	80.4
	Straws	1.3	1.55	1.89	60	65.9	81.2	86.6	88
	Lids	1.12	1.5	1.91	62.3	68.3	78.5	82.8	86.1
	Cylinder foams	1.2	1.71	1.98	55.6	68.6	86.5	88.1	90.2

height is fixed, the metric increases with frequency. This holds true for both the test cases and thresholds. This means that the increase in water waves height and MW frequencies lead to higher backscatter intensity signals. The presence of the scattered, floating macroplastics items further contributes towards the increase in backscattered intensity. This verifies the previous simulation analysis behavior and corroborates the previous ML results using a wider 1 GHz.
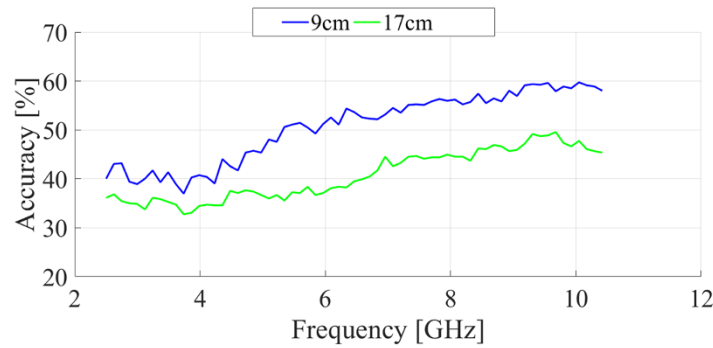
Next, we analyze the performance of the MLP considering the narrower EESS intervals. Columns 4–8 of Table 3 show the detection accuracy obtained using only steps 3 and 4 of the supervised learning workflow. For both 9 and 17 cm test cases, the performance using ML accompanies the *EnR* metric, increasing with MW frequency and worsening with the increase in water wave heights. Albeit slightly lower, these accuracy results agree with the supervised workflow results discussed previously in the "Detection analysis" subsection that use a wider 1 GHz. As we narrow the frequency interval, we limit the number of features considered by the ML model and, consequently, possibly exclude MW frequencies with a resonant scattering response for the detection. Still, the accuracy results maintain the relationship with water wave height and MW frequency, i.e., decrease and increase, respectively. Additionally, except for the 9-cm plastic bottles and lids cases, the last column of Table 3 shows that the consideration of the noncontiguous EESS frequency intervals can lead to better detection results. Accordingly, this improvement is justified because the detection performance benefits from adding more (optimal) X-band frequency information as features of the model.

This analysis shows that the *EnR* metric and the MLP model obtain compatible results. On one hand, *EnR* provides physical interpretability in terms of the excess scattered energy in the presence of plastic, but at the cost of bandwidth, need for an unpractical reference measurement and need of sequential measurements of the same scenario to capture targets drift (although the latter can be obtained with spotlight mode [41]). On the other hand, ML automation can consider standard EESS bands and shuffled input signals when training the model. This leads to a more robust detection performance that can be adapted for fast-changing deep-sea scenarios, suitable for real-time monitoring.

Multiclass analysis

Thus far, the analysis considered the datasets of each type of target at a time (either bottles, or straws, or lids, or foam). In this subsection, we evaluate if can use supervised ML to differentiate between the different plastic targets.

We apply the supervised ML workflow to merged datasets of the four types of targets (see the "Supervised learning workflow" subsection) and perform multiclass classification to distinguish between them. We test cases for 9 and 17 cm water wave heights. We show in Fig. 11(a) the accuracy output of this multiclass scenario. In neither the 9 nor 17 cm water wave height cases, did the maximum accuracy reach a high enough value for detection. Still, similarly to binary classification, we observe an identical trend in accuracy with respect to MW frequency and water wave height: accuracy increases with MW frequency but decrease with water

Figure 11. (a) Multiclass classification accuracy output for supervised learning workflow using 1 GHz sub-bands for the test cases with an H_s of 9 and 17 cm; (b) confusion matrix for highest accuracy output of the 9 cm case; (c) confusion matrix for highest accuracy output of the 17 cm case.

wave height. To further investigate the low accuracy results, we present in Fig. 11(b) and 11(c) the confusion matrices for the optimal detection case (maximum accuracy) for 9 and 17 cm water wave height cases, respectively.

First, let us consider the 9 cm test cases. While the reference measurements are mostly correctly classified, most of the four types of target measurements are incorrectly classified. This means that the MLP model easily separates reference measurements from target ones (seen already with the previous detection analysis), but it struggles to confidently discriminate between the different target measurements. This explains the low accuracy output when predicting on the unseen data.

For the 17 cm wave case, we observe an increase in misclassified references and target measurements, particularly for the plastic bottles and straws classes. As the water wave height increases, the MLP model struggles to define multiple decision boundaries, making it difficult to differentiate between targets. The scattering intensity across the MW spectrum from the target measurements is already very similar in the lower wave height case, and the increase in wave height further reduces this distinction. This is because the scattering intensity from the water surface increases, which

deteriorates the detection sensitivity for the different types of plastic items. Hence, the results indicate that even with the use of the optimal X-band frequencies, multiclass classification is reduced to a binary one.

Conclusions

This study demonstrated that ML can be used to identify in experiments, the optimal MW frequencies to detect the presence of typical single-use floating macroplastics, spread at low concentrations ($10 \ g/m^2$) across the water surface. Furthermore, the possibility of using ML to process MW data at signal level, allows for a fast analysis that can complement other detection metrics in coarse and fast changing environments.

We verified through numerical analysis that the intensity of the backscatter signal depends on the interplay between the depth and size of the water indentation beneath the otherwise practically transparent floating target, and the wavelength of the MW signal. At MW frequencies, each floating macroplastic target tends to have higher backscatter response near resonances. Simulation work emulating the experimental measurements showed that the

presence of the floating macroplastic targets maximizes detection probability at X-band in comparison to S- and C-bands.

This result corroborated the experimental characterization of the frequency dependent scattering behavior obtained in the previous exploratory analysis through the unsupervised workflow [25]. For all the measured test cases, the presence of the scattered plastic litter targets increased the importance of X-band frequencies (particularly above 8 GHz). Using the proposed supervised learning workflow we identified these X-band frequencies as optimal for detection, obtaining accuracies of at least 90% and 80% for the lower and higher water wave height datasets, respectively. Additionally, we verified that detection sensitivity is worsened with increasing water wave height, with detection performance least deteriorated when using the optimal X-band frequencies.

The study also showed that the multiclass classification, i.e., distinguishing between different plastic items, is reduced to a binary one, worsening at higher wave heights. This is explained by the identified scattering mechanism based on the water indentation rather than the shape and scarce amount of plastic of the typical single-use items.

In comparison to the alternative *EnR* radar-based metric, the use of ML obtained comparable detection performance, showing to be effective whilst overcoming the *EnR* requirement of threshold determination and the necessity of using wider bandwidth. We outlined the further advantage of ML to leverage the frequency dependent scattering mechanism across the MW spectrum by adding optimal, noncontiguous, narrower EESS bands. These advantages are the crucial for implementing a real-time time sensing service using existing (or even future) missions.

Future work will address the lack of high-quality MW data to further study detection dependencies and consider alternative architectures and learning strategies to improve generalization capability of ML for outdoor scenarios with changing water spectrums and limited experimental data.

Competing interests. The authors declare no conflict of interest.

References

1. **Maximenko N, Corradi P, Law KL, Van Sebille E, Garaba SP, Lampitt RS … Wilcox C** (2019) Toward the integrated marine debris observing system. *Frontiers in Marine Science* **6**. doi:10.3389/fmars.2019.00447

2. **Salgado-Hernanz PM, Bauzà J, Alomar C, Compa M, Romero L and Deudero S** (2021) Assessment of marine litter through remote sensing: Recent approaches and future goals. *Marine Pollution Bulletin* **168**(112347), 112347. doi:10.1016/j.marpolbul.2021.112347

3. **Goddijn-Murphy L, Peters S, van Sebille E, James NA and Gibb S** (2018) Concept for a hyperspectral remote sensing algorithm for floating marine macro plastics. *Marine Pollution Bulletin* **126**, 255–262. doi:10.1016/j.marpolbul.2017.11.011

4. **Moy K, Neilson B, Chung A, Meadows A, Castrence M, Ambagis S and Davidson K** (2018) Mapping coastal marine debris using aerial imagery and spatial analysis. *Marine Pollution Bulletin* **132**, 52–59. doi:10.1016/j.marpolbul.2017.11.045

5. **Tasseron P, van Emmerik T, Peller J, Schreyers L and Biermann L** (2021) Advancing floating macroplastic detection from space using experimental hyperspectral imagery. *Remote Sensing* **13**(12), 2335. doi:10.3390/rs13122335

6. **Evans MC and Ruf CS** (2022) Toward the detection and imaging of ocean microplastics with a spaceborne radar. *IEEE Transactions on Geoscience and Remote Sensing: A Publication of the IEEE Geoscience and Remote Sensing Society* **60**, 1–9. doi:10.1109/tgrs.2021.3081691

7. **Basu B, Sannigrahi S, Sarkar Basu A and Pilla F** (2021) Development of novel classification algorithms for detection of floating plastic debris in coastal waterbodies using multispectral Sentinel-2 remote sensing imagery. *Remote Sensing* **13**(8), 1598. doi:10.3390/rs13081598

8. **Gnann N, Baschek B and Ternes TA** (2022) Close-range remote sensing-based detection and identification of macroplastics on water assisted by artificial intelligence: A review. *Water Research* **222**(118902), 118902. doi:10.1016/j.watres.2022.118902

9. **Jia T, Kapelan Z, de Vries R, Vriend P, Peereboom EC, Okkerman I and Taormina R** (2023) Deep learning for detecting macroplastic litter in water bodies: A review. *Water Research* **231**(119632), 119632. doi:10.1016/j.watres.2023.119632

10. **Felício JM, Costa TS, Vala M, Leonor N, Costa JR, Marques P and de Maagt P** (2024) Feasibility of radar-based detection of floating macroplastics at microwave frequencies. *IEEE Transactions on Antennas and Propagation* **72**(3), 2766–2779. doi:10.1109/tap.2023.3347031

11. **Davaasuren N, Marino A, Boardman C, Alparone M, Nunziata F, Ackermann N and Hajnsek I** (2018) Detecting microplastics pollution in world oceans using Sar remote sensing. IGARSS 2018 - 2018 IEEE International Geoscience and Remote Sensing Symposium. Presented at the IGARSS 2018 - 2018 IEEE International Geoscience and Remote Sensing Symposium. Valencia. doi:10.1109/igarss.2018.8517281

12. **Topouzelis K, Papageorgiou D, Karagaitanakis A, Papakonstantinou A and Ballesteros MA** (2020) Plastic litter project 2019: Exploring the detection of floating plastic litter using drones and sentinel 2 satellite images. IGARSS 2020 - 2020 IEEE International Geoscience and Remote Sensing Symposium. Presented at the IGARSS 2020 - 2020 IEEE International Geoscience and Remote Sensing Symposium. Waikoloa, HI, USA. doi:10.1109/igarss39084.2020.9324548

13. **Vala M, Felício JM, Da Costa TS, Leonor N, Costa JR, Marques P and de Maagt P** (2023) On the feasibility of using passive mm-wave imaging for marine litter detection at the W-band. 17th European Conference on Antennas and Propagation (EuCAP). Florence, Italy. doi:10.23919/eucap57121.2023.10133069

14. **Da Costa TS, Felício JM, Vala M, Leonor N, Costa JR, Marques P and de Maagt P** (2023) Detection of low permittivity floating plastic sheets at microwave frequencies. 17th European Conference on Antennas and Propagation (EuCAP). Florence, Italy. doi:10.23919/eucap57121.2023.10133107

15. **Serafino F and Bianco A** (2024) X-band radar detection of Small Garbage Islands in different sea state conditions. *Remote Sensing* **16**(12), 2101. doi:10.3390/rs16122101

16. **Amani M, Moghimi A, Mirmazloumi SM, Ranjgar B, Ghorbanian A, Ojaghi S and Jin S** (2022) Ocean Remote Sensing techniques and applications: A review (part I). *Water* **14**(21), 3400. doi:10.3390/w14213400

17. **Xiang K, Zhou W and Bao Q** (2024) Sea surface wind speed estimation from the combination of satellite scatterometer and radiometer parameters. *Journal of Geophysical Research: Machine Learning and Computation* **1**(3). doi:10.1029/2024jh000165

18. **Gao D, Liu Y, Meng J, Jia Y and Fan C** (2018) Estimating significant wave height from SAR imagery based on an SVM regression model. *Hai Yang Xue Bao [Acta Oceanologica Sinica]* **37**(3), 103–110. doi:10.1007/s13131-018-1203-7

19. **Krinitskiy MA, Golikov VA, Anikin NN, Suslov AI, Gavrikov AV and Tilinina ND** (2023) Estimating significant wave height from X-band navigation radar using convolutional neural networks. *Moscow University Physics Bulletin* **78**(S1), S128–S137. doi:10.3103/s0027134923070159

20. **Leigh S, Wang Z and Clausi DA** (2014) Automated ice–water classification using dual polarization SAR satellite imagery. *IEEE Transactions on Geoscience and Remote Sensing: A Publication of the IEEE Geoscience and Remote Sensing Society* **52**(9), 5529–5539. doi:10.1109/tgrs.2013.2290231

21. **Xing X, Ji K, Zou H and Sun J** (2013) Feature selection and weighted SVM classifier-based ship detection in PolSAR imagery. *International Journal of Remote Sensing* **34**(22), 7925–7944. doi:10.1080/01431161.2013. 827812

22. **Somaraju R and Trumpf J** (2006) Frequency, temperature and salinity variation of the permittivity of seawater. *IEEE Transactions on Antennas and Propagation* **54**(11), 3441–3448. doi:10.1109/tap.2006.884290

23. **Lebreton L, Slat B, Ferrari F, Sainte-Rose B, Aitken J, Marthouse R, Hajbane S, Cunsolo S, Schwarz A, Levivier A and Noble K** (2018) Evidence that the Great Pacific Garbage Patch is rapidly accumulating plastic. *Scientific Reports* **8**, 4666. doi:10.1038/s41598-018-22939-w

24. **Enabling delta life** (2024) DELTARES wave facility [Online]. Available at: https://www.deltares.nl/en (accessed 10 November 2024).

25. **Da Costa TS, Felício JM, Vala M, Leonor N, Costa JR, Marques P and De Maagt P** (2024) Feature selection for identifying optimal microwave frequencies to detect floating macroplastic litter in C and X bands. 18th European Conference on Antennas and Propagation (EuCAP). Glasgow, United Kingdom. doi:10.23919/eucap60739.2024.10501024.

26. **Kim SB and Rattakorn P** (2011) Unsupervised feature selection using weighted principal components. *Expert Systems with Applications* **38**(5), 5704–5710. doi:10.1016/j.eswa.2010.10.063

27. **Denimal -J-J and Camiz S** (2022) Complex principal component analysis: Theory and geometrical aspects. *Journal of Classification* **39**(2), 376–408. doi:10.1007/s00357-022-09412-0

28. **Jolliffe IT and Cadima J** (2016) Principal component analysis: A review and recent developments. *Philosophical Transactions of the Royal Society A: Mathematical, Physical and Engineering Sciences* **374**(2065), 20150202. doi:10.1098/rsta.2015.0202.

29. **Song F, Guo Z and Mei D** (2010) Feature selection using principal component analysis. 2010 International Conference on System Science, Engineering Design and Manufacturing Informatization. Presented at the 2010 International Conference on System Science, Engineering Design and Manufacturing Informatization (ICSEM). Yichang, China. doi:10.1109/icsem.2010.14

30. **Felício JM, Bioucas-Dias JM, Costa JR and Fernandes CA** (2019) Antenna design and near-field characterization for medical microwave imaging applications. *IEEE Transactions on Antennas and Propagation* **67**(7), 4811–4824. doi:10.1109/TAP.2019.2905742

31. **Goodfellow I, Bengio Y, and Courville A** (2018) *Deep Learning*, Vol. 1. No. 2. Cambridge: MIT press.

32. **Gorishniy Y, Rubachev I, Khrulkov V, and Babenko A** (2021) *Revisiting Deep Learning Models for Tabular Data*, Vol. 34. Advances in Neural Information Processing Systems. Curran Associates, Inc. doi:10.48550/ARXIV.2106.11959

33. **Hirose A** (ed.), (2013) *Complex-valued Neural Networks*. Berlin Heidelberg: Springer. doi:10.1002/9781118590072

34. **Barrachina JA, Ren C, Vieillard G, Morisseau C and Ovarlez Jp** (2021) About the equivalence between complex-valued and real-valued fully connected neural networks-application to PolInSAR images. IEEE 31st International Workshop on Machine Learning for Signal Processing (MLSP). IEEE.

35. **GESAM** (2019) Guidelines For The Monitoring And Assessment Of Plastic Litter In The Ocean. Nº99, United Nations Environment Programme (UNEP).

36. **Hasselmann K and Olbers D** (1973) Measurements of wind-wave growth and swell decay during the Joint North Sea Wave Project (JONSWAP). *Ergaenzungsheft Zur Deutschen Hydrographischen Zeitschrift, Reihe A* **8**(12), 1–95.

37. **Liaw R, Liang E, Nishihara R, Moritz P, Gonzalez JE and Stoica I** (2018) Tune: A research platform for distributed model selection and training. arXiv preprint arXiv:1807.05118.

38. **International Telecommunication Union ITU** 2015 Radio ITU Radio Regulatory Framework for Space Services. Available at: https://www.itu.int/en/ITU-R/space/snl/Documents/ITU-Space_reg.pdf (accessed 12 May 2025).

39. **CST studio suite** (2024) 3D EM Simulation and Analysis software. [Online]. Available: http://www.cst.com/ (accessed 13 Januray 2025).

40. **Bethe HA** (1944) Theory of diffraction by small holes. *Physical Review* **66**(7-8), 163. doi:10.1103/PhysRev.66.163.

41. **Belcher DP and Baker CJ** (1996) High resolution processing of hybrid strip-map/spotlight mode SAR. *IEE Proceedings-Radar, Sonar and Navigation* **143**(6), 366–374. doi:10.1049/ip-rsn:19960790.

Appendix

Our tuning protocol employs a nested cross-validation (CV) approach. Initially, we partition the data into fivefolds, and each of these folds is used for hyperparameter tuning. Each trial, i.e., hyperparameter combination sampled from the search space of Table 1, is evaluated in each fold. The accuracy results from the left out validation subset in each fold are then averaged to output the performance under a specific hyperparameter combination. The optimal hyperparameter combination is the one that outputs the maximum average accuracy from the left out validation subsets of the CV approach. This process is repeated considering the domain mapping ($\mathbb{C} \to \mathbb{R}$) of complex to real at the input and output layers of the model.

For hyperparameter optimization (HPO), we utilize the *Ray Tune* framework [37], a well-known HPO library with the Tree-structured Parzen Estimator (TP) algorithm for HPO, the default HPO method. The optimization is constrained by a budget of either 50 trials, i.e., a combination of hyperparameters, or a maximum duration of 23 h. To enhance efficiency, we executed every trial in parallel across all test cases. All experiments were run on NVIDIA GeForce GTX 1050 Ti GPU with a memory of 16 GB.

Table A1. Search space for the MLP model

Parameter	Type	Range
Nº HLs	Integer	[1, 4]
Nº Hidden Neurons	Integer	[16,128]
Batch Size	Integer	{8,16,32}
Activation Function	Categorical	{ReLU, LeakyReLU, Tanh, Linear, PReLU}
Dropout	Float	[0,1]
Learning Rate	Float	$[10^{-6},10^{-1}]$
Weight Decay	Float	$[10^{-6},10^{-3}]$

Tomás Soares da Costa was born in Lisbon, Portugal, in 1996. He received the bachelor and a dual M.Sc. degree in electrical and computer engineering from the Instituto Superior Técnico (IST), University of Lisbon, Lisbon, Portugal, and Kungliga Tekniska Högskolan (KTH) Royal Institute of Technology, Stockholm, Sweden in 2017 and 2019, respectively. He is currently pursuing the Ph.D. degree in electrical and computer engineering under the theme "Microwave detection of floating marine plastic using machine learning" with the IST, University of Lisbon, Lisbon, Portugal. He is currently a Researcher with the Antennas & Propagation (A&P-Lx) Research Group, Instituto de Telecomunicações (IT), Lisbon, and Teaching Assistant (TA) for the Deep Learning course at IST. His current interests include radar signal processing, radiowave propagation, microwave and radiofrequency engineering, deep learning and machine learning applied to electromagnetics.

João M. Felício received the M.Sc. and Ph.D. degrees in Electrical and Computer Engineering from Instituto Superior Técnico (IST), University of Lisbon, Lisbon, Portugal, in 2014 and 2018, respectively. He is currently Assistant Professor with the Electrical and Computer Engineering Department at IST, and a Researcher with Instituto de Telecomunicações, Lisbon. He has co-authored more than 100 technical papers in peer-reviewed international journals and conference proceedings. His current interests include microwave imaging and remote sensing, mm-wave antenna design,

namely transmitarray and reflectarray antennas, complex permittivity measurement techniques, and machine learning applied to microwave remote sensing.

Mário Vala was born in Leiria, Portugal, in 1996. He received the bachelor's degree in electrical and computer engineering, electronics & computers, and the M.Sc. degree in electrical engineering, electronics & telecommunications, from the School of Technology and Management (ESTG), Polytechnic Institute of Leiria (IPL), Leiria, in 2017 and 2019, respectively. He is currently pursuing the Ph.D. degree under the theme "Radiowave Propagation in Wildfires" with the Instituto Superior Técnico, University of Lisbon, Lisbon, Portugal. He is currently a Researcher with the Antennas & Propagation (A&P-Lr) Research Group, Instituto de Telecomunicações, Leiria.

Rafael F. S. Caldeirinha (Senior Member, IEEE) was born in Leiria, Portugal, in 1974. He received the B.Eng. degree in electronic and communication engineering and the Ph.D. degree from the University of Glamorgan, Pontypridd, U.K., in 1997 and 2001, respectively, and the Habilitation degree from the University of Aveiro, Aveiro, Portugal, in 2020. He is a Senior Researcher and the Head of the Antennas & Propagation (A&P-Lr) Research Group, Instituto de Telecomunicações, Leiria, since 2010, and a Coordinator Professor of mobile communications with the Polytechnic of Leiria, Leiria, since 2001. He has authored or coauthored more than 190 papers in conferences and international journals, and four contributions to the ITU-R Study Group, which formed the basis of the ITU–R P.833–5 (2005) recommendation. His research interests include studies of radiowave propagation through vegetation media, including wildfires, radio channel sounding and modeling, and frequency-selective surfaces, for applications at microwave and millimeter-wave frequencies.

Sérgio A. Matos (Senior Member, IEEE) received the Licenciado, M.Sc., and Ph.D. degrees in electrical and computer engineering from the Instituto Superior Técnico (IST), University of Lisbon, Lisbon, Portugal, in 2004, 2005, and 2010, respectively. He is currently a Researcher with the Instituto de Telecomunicações (IT), Lisbon. He is also an Assistant Professor with habilitation at the Departamento de Ciências e Tecnologias da Informação, Instituto Universitário de Lisboa (ISCTE-IUL). He is the coauthor of more than 110 technical papers in international journals and conference proceedings. His current research interests include millimeter-wave design for 5G and 6G applications

Jorge R. Costa (Senior Member, IEEE) was born in Lisbon, Portugal, in 1974. He received the Licenciado and Ph.D. degrees in electrical and computer engineering from the Instituto Superior Técnico (IST), Technical University of Lisbon, Lisbon, Portugal, in 1997 and 2002, respectively. He is currently a Senior Researcher at the Instituto de Telecomunicações, Lisbon, Portugal and a Full Professor at the Departamento de Ciências e Tecnologias da Informação, Instituto Universitário de Lisboa (ISCTE-IUL). His present research interests include dielectric lenses, transmit-arrays, and biomedical antennas.

He is the co-author of four patent applications and more than 250 contributions to peer-reviewed journals and international conference proceedings. Prof. Costa served as an Associate Editor for the *IEEE Transactions on Antennas and Propagation* from 2010 to 2016. He is currently an Associate Editor of the *IEEE Open Journal of Antennas and Propagation*.

Carlos A. Fernandes (Life Senior Member, IEEE) received the Licenciado, M.Sc., and Ph.D. degrees in electrical and computer engineering from the Instituto Superior Técnico (IST), Technical University of Lisbon, Lisbon, Portugal, in 1980, 1985, and 1990, respectively. He joined IST in 1980, where he is currently a Full Professor of microwaves, radio wave propagation, and antennas with the Department of Electrical and Computer Engineering. He is a Senior Researcher with the Instituto de Telecomunicações, Leiria, Portugal, where he is a member of the Board of Directors. He has coauthored one book, three book chapters, more than 250 technical papers in peer-reviewed international journals and conference proceedings, and seven patents in the areas of antennas and radio wave propagation modeling. His current research interests include antennas for millimeter-wave applications in 5G and satellite communications, RFID and ultrawideband (UWB) antennas for the Internet of Things (IoT), metamaterials, and medical microwave imaging.

Nelson J. G. Fonseca (IEEE Fellow) received the M.Eng. degree from Ecole Nationale Supérieure d'Electrotechnique, Electronique, Informatique, Hydraulique et Télécommunications (ENSEEIHT), Toulouse, France, in 2003, the M.Sc. degree from the Ecole Polytechnique de Montreal, Quebec, Canada, also in 2003, and the PhD degree from Institut National Polytechnique de Toulouse – Université de Toulouse, France, in 2010, all in electrical engineering. He currently works as Chief Innovation Officer for Anywaves, Toulouse, France, contributing to the development of their custom space-segment antennas portfolio. He is also the founding director of 3SPACE Innovation, Paris, France, a consulting company providing support on novel ground-segment and terrestrial wireless communication antenna systems. His research interests include multiple beam antennas for space missions, beamformer theory and design, ground terminal antennas and novel manufacturing techniques. He has authored or co-authored more than 330 papers in peer-reviewed journals and conferences and has over 50 patents issued or pending.

Peter de Maagt was born in Pauluspolder, The Netherlands, in 1964. He received the M.Sc. and Ph.D. degrees in electrical engineering from Eindhoven University of Technology, Eindhoven, The Netherlands, in 1988 and 1992, respectively. Currently, he is with the European Space Research and Technology Centre (ESTEC), European Space Agency (ESA), Noordwijk, The Netherlands. His research interests include the areas of millimeter wave reflector, quasi-optics, electromagnetic bandgap antennas, and millimeter- and submillimeter-wave components. He was the co-recipient of the H. A. Wheeler Award of the IEEE Antennas and Propagation Society for the Best Applications Paper of 2001 and 2008. He was granted an ESA Award for Innovation in 2002, and an ESA award for Corporate Team Achievements for the Herschel and Planck program in 2010. He was the co-recipient of Best Paper Awards at the 2006 Loughborough Antennas Propagation Conference (LAPC) and 2007 the International Workshop on Antenna Technology (IWAT).